

Vibrations of free and surface-coupled atomic force microscope cantilevers: Theory and experiment

U. Rabe, K. Janser, and W. Arnold

Fraunhofer Institute for Nondestructive Testing (IZP), University, D-66123 Saarbruecken, Germany

(Received 25 March 1996; accepted for publication 3 June 1996)

With an optical interferometer, the free vibration spectra and the local vibration amplitude of four rectangular atomic force microscope cantilevers made of silicon have been examined experimentally in a spectral range of 100 kHz to 10 MHz. A good agreement with the exural wave theory of elastic beams was found. Coupling to torsional vibrations was also observed. When the sensor tip of the cantilever is in contact with a sample surface the resonances are shifted in frequency and the vibration amplitudes along the cantilever change. A method is presented to calculate this frequency shift using a linear approximation for the tip-sample interaction forces, and the results are compared with the frequency shift calculated from the point-mass model. The measured resonance frequencies of a surface-coupled cantilever do not correspond as well to the theoretical ones as in the free case even if the elastic-beam model is used. The reason for the disagreement is found to be the geometry of the commercial cantilevers and the nonlinearity of the tip-sample interaction force. © 1996 American Institute of Physics. [S034-6748(96)02809-2]

I. INTRODUCTION

In the original atomic force microscope (AFM)¹ the topography of a sample surface is imaged by scanning a sharp sensor tip fixed to a soft cantilever over the sample surface and by measuring the cantilever deflection. As there is a demand to measure surface properties such as adhesive energy or sample stiffness with the same high local resolution as the topography, dynamic methods such as force modulation microscopy,² tapping mode,³ or atomic force acoustic microscopy^{4–6} have been developed. In these techniques, the cantilever vibrates while it is scanned across the surface with the sensor tip in contact with the sample surface at least during a fraction of its vibration cycle. All these methods reveal changes in contrast when different materials are present on the sample surface. A quantitative interpretation of the images, however, is difficult because two different phenomena are involved which cannot be expressed in simple equations: the tip-sample interaction force and the cantilever vibration.

It is well known that an AFM cantilever is a miniature elastic beam with its characteristic vibration modes and frequencies.^{7,8} Resonance frequencies of higher modes of AFM cantilevers have been measured by different groups^{8–10} and higher vibration modes were used for imaging.^{5,9,10} The local vibration amplitude of the third and fourth bending mode of a 23.5-mm-long rectangular cantilever made of glass with metal coating was measured with a beam deflection sensor.¹¹ The static and dynamic deflection of cantilevers with triangular shape was examined experimentally and numerically,^{12–15} and the thermal noise of a rectangular cantilever was calculated considering all possible exural vibration modes.¹⁶

However, for vibration techniques which use frequencies around or below the first exural vibration frequency of the cantilever, the elastic-beam model is commonly replaced by the much simpler point-mass model. As will be shown here, the point-mass model comes to its limits when the vibration

amplitude along the cantilever changes; therefore an incorrect frequency shift of the fundamental mode is obtained if the tip-sample contact stiffness is higher than the spring constant of the cantilever. A quantitative calculation of the resonance frequencies is important when quantitative information—for example, about sample surface elasticity or adhesion energy—is to be extracted from the images.

II. FREE AFM CANTILEVERS

A. Calculation of exural vibrations of free rectangular AFM cantilevers

While the vibration modes of cantilevers with variable cross section such as the widely used triangular cantilevers require numerical calculations,^{12–15} the theory becomes simpler for cantilevers with homogeneous cross section, such as rectangular ones. The equation of motion for exural vibrations and its solutions for the clamped-free cantilever can be found in textbooks on acoustics^{17,18} and also in the AFM literature,^{7,8} and is therefore only briefly summarized here.

For a homogeneous beam of uniform cross section, the equation of motion for exural vibrations is a differential equation of fourth order:

$$EI \frac{\partial^4 y}{\partial x^4} + \rho A \frac{\partial^2 y}{\partial t^2} = 0, \quad (1)$$

where E is the modulus of elasticity, ρ is the mass density, $A = a \cdot b$ is the cross section, and I is the area moment of inertia. a and b are the width and the thickness of the cantilever, respectively. The area moment is $I = ab^3/12$ in the case of a beam with rectangular cross section. x is the coordinate in the longitudinal direction of the cantilever as shown in Fig. 1(a). $y(x)$ is the deflection from the rest position of the length element at x , $\partial y/\partial x$ is the slope, $EI \cdot \partial^2 y/\partial x^2$ is the moment, and $EI \cdot \partial^3 y/\partial x^3$ is the shear force at x . A general solution of the type

$$y(x,t) = (a_1 e^{kx} + a_2 e^{-kx} + a_3 e^{ikx} + a_4 e^{-ikx}) e^{-imt} \quad (2)$$

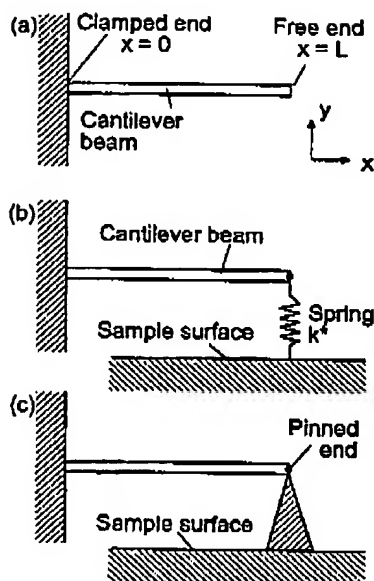


FIG. 1. Boundary conditions of an AFM cantilever with uniform cross section: (a) Clamped-free cantilever, (b) clamped spring-coupled cantilever, (c) clamped-pinned cantilever.

with wave number $k = 2\pi/\lambda$, and angular frequency $\omega = 2\pi f$ can be obtained by inserting Eq. (2) into Eq. (1) yielding the following dispersion relation:

$$EI \cdot k^4 - \rho A \cdot \omega^2 = 0. \quad (3)$$

a_i ($i = 1, 2, 3, 4$) are constants. Since the cantilever beam is of finite length L , boundary conditions have to be fulfilled by the solutions of Eq. (3). If the cantilever is clamped at one end and free at the other end, as is the case for an AFM cantilever without sample contact, the deflection and the slope have to vanish at the clamped end ($x=0$), and no moment and shear force can be present at the free end ($x=L$):

$$y=0, \quad \frac{\partial y}{\partial x}=0 \quad \text{for } x=0$$

and

$$\frac{\partial^2 y}{\partial x^2}=0, \quad \frac{\partial^3 y}{\partial x^3}=0 \quad \text{for } x=L. \quad (4)$$

The general solution and its derivatives are inserted into Eq. (4). The resulting four equations can be solved for the coefficients a_i only if the characteristic equation

$$\cos k_n L \cosh k_n L + 1 = 0 \quad (5)$$

is fulfilled. The solutions $\{k_n L, n=1, 2, \dots\}$ of this equation give the wave numbers k_n of an infinite set of exural vibration modes, where n is the mode number. With the help of the dispersion relation Eq. (3), the resonance frequency f_n belonging to k_n can be calculated:

$$f_n = \frac{(k_n L)^2}{c_c^2}, \quad (6)$$

with

$$c_c = L \sqrt{2\pi} \sqrt{\frac{\rho A}{EI}}. \quad (7)$$

c_c is a constant containing the geometrical dimensions, Young's modulus, and the density of the cantilever. The deflection $y_n(x)$ of each mode is described by the following equation:

$$y_n(x) = y_0 \left(\cos k_n x - \cosh k_n x \right) - \frac{\cos k_n L + \cosh k_n L}{\sin k_n L + \sinh k_n L} \left(\sin k_n x - \sinh k_n x \right), \quad (8)$$

where y_0 is the vibrational amplitude.

B. Comparison to the point-mass model

In the point-mass model, the elastic beam is replaced by a point mass m^* attached to a spring with stiffness k_c . m^* is chosen such that the resonance frequency of the system

$$\omega_0 = \sqrt{k_c/m^*} \quad (9)$$

is equal to the lowest exural vibration frequency ω_1 . The spring constant k_c of a rectangular cantilever is⁷

$$k_c = \frac{Eb^3 a}{4L^3} \quad (10)$$

and the lowest exural vibration frequency is obtained from Eqs. (6) and (7) by setting $n=1$:

$$\omega_1 = k_1^2 \sqrt{\frac{EI}{\rho A}} = (1.875)^2 \frac{1}{L^2} \sqrt{\frac{Eb^2}{12\rho}}. \quad (11)$$

m^* can now be calculated directly from Eqs. (10) and (11), yielding

$$m^* = \frac{k_c}{\omega_1^2} = \frac{3\rho Lab}{(1.875)^4} \approx \frac{1}{4} m. \quad (12)$$

The effective mass m^* of a rectangular cantilever is about one-quarter of its real mass m . This also means that the lowest resonance frequency of a beam with a mass m_{tip} attached to its end is

$$\omega_{tip} \approx \sqrt{\frac{k_c}{\frac{m}{4} + m_{tip}}}. \quad (13)$$

C. Other vibration modes

Apart from exural vibrations in the y direction [Fig. 1(a)], in principle, exural vibrations can also be excited in the direction perpendicular to y and x (z direction). Also, longitudinal vibrations and Lamb modes are possible. For common AFM cantilevers, the resonance frequencies, however, of these modes are much higher than the resonance

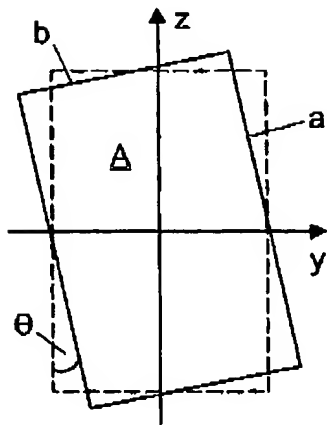


FIG. 2. Under torsional vibrations the cross section area A of a rectangular cantilever with thickness b and width a is rotated by an angle θ .

frequencies of the flexural vibrations in the y direction. Additionally, most position detectors, such as beam deflection sensors, are not sensitive to movements in the $x-z$ plane. Torsional vibrations, however, cause deflections in the y direction and can have lower resonance frequencies. The equation of motion is a differential equation of second order¹⁸:

$$C \frac{\partial^2 \theta}{\partial x^2} = \rho J \frac{\partial^2 \theta}{\partial x^2}. \quad (14)$$

θ is the angle of torsion of the cross-section area (see Fig. 2), C is the torsional stiffness, ρ is the mass density, and J is the polar area moment of inertia. If the cross section is rectangular, the polar moment of inertia can be calculated as follows:

$$J = 4 \int_0^{a/2} \int_0^{b/2} (z^2 + y^2) dy dz = \frac{1}{12} (a^3 b + b^3 a) \approx \frac{a^3 b}{12}. \quad (15)$$

The term containing b^3 can be neglected because usually $a \gg b$. In the case $a \gg b$ the torsional stiffness C is¹⁹

$$C = \frac{ab^3}{3} G, \quad (16)$$

where G is the shear modulus of the cantilever. Again, a harmonic solution is assumed and the boundary conditions for the clamped-free cantilever are inserted. Since the differential equation for torsional vibrations is only of second order, the phase velocity v is a constant and the modes are equidistant in frequency:

$$v = \lambda f = \sqrt{\frac{C}{\rho J}} = 2 \frac{b}{a} \sqrt{\frac{G}{\rho}}, \quad (17)$$

$$f_n = \frac{2n-1}{2L} \frac{b}{a} \sqrt{\frac{G}{\rho}}. \quad (18)$$

The lowest torsional vibration frequencies are about ten times higher than the flexural frequencies for typical AFM cantilevers. Torsional movements of the cantilever below its

first resonance frequency are used in the lateral force mode,²⁰ where frictional forces between tip and surface are measured.

D. Measurement of free AFM-cantilever vibrations

We examined vibrations of free AFM cantilevers experimentally. This was done with the setup shown schematically in Fig. 3. By oscillating the clamped end, forced cantilever vibrations are excited. The base of the cantilever, a chip measuring $2 \times 4 \times 0.5 \text{ mm}^3$, is glued with coupling gel to an ultrasonic transducer. The transducer is excited with continuous rf in the frequency range of 100 kHz to 10 MHz. It emits longitudinal waves which are transmitted into the chip and therefore cause vibrations of the clamped cantilever end. The absolute amplitude of the cantilever vibrations is measured with an optical Michelson heterodyne interferometer.²¹ The He-Ne laser beam of the interferometer is focused onto the cantilever with a microscope objective with a focal length of 16.9 mm. Thus, a focal spot diameter of approximately $5 \mu\text{m}$ is achieved, much smaller than the cantilever width. The laser beam is backscattered from the cantilever and interferes with a reference beam in the interferometer which is frequency-shifted by 160 MHz relative to the signal beam. The interference signal is detected by a fast photodiode, amplified by 60 dB and demodulated. Calibrated amplitude detection is possible above about 100 kHz, the upper frequency of the phase-locked feedback loop of our demodulation unit.²² To improve the signal-to-noise ratio, a low pass filter of 28 MHz was used. The filtered signal is displayed by a fast digital oscilloscope of 150 MHz bandwidth. Furthermore, averaging of up to 200 vibration cycles and fast Fourier transforming in order to examine the frequency spectrum of the signals are possible. The transducer with the chip is mounted on a motor-driven linear translation stage with a smallest step size of $0.5 \mu\text{m}$. In this way the focal spot of the interferometer can be scanned along the cantilever.

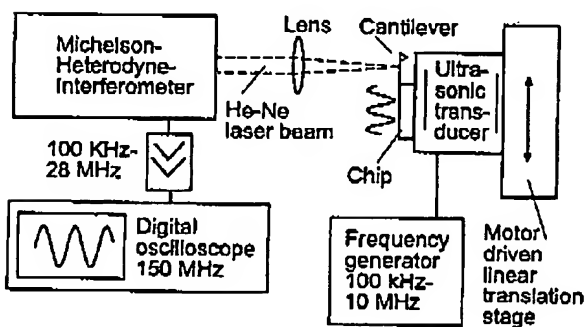


FIG. 3. Experimental setup to measure the free AFM-cantilever vibrations. The chip with the cantilever is glued to an ultrasonic transducer. The transducer is excited with rf in the frequency range 100 kHz to 10 MHz. It emits compressional waves which are coupled into the chip and excite forced cantilever vibrations by vibrations of the clamped end of the cantilever. To measure the cantilever vibrations, the He-Ne laser beam of an optical Michelson heterodyne interferometer is focused onto the cantilever. The signals of the interferometer are amplified and fed to the input channel of a fast digital oscilloscope. With a motor driven linear translation stage, the sensor spot of the interferometer is scanned along the cantilever.

TABLE I. Data of the rectangular cantilevers made of monocrystalline silicon (Ref. 16) used in the experiments.

	Cantilever			
	1	2	3	4
Length (L_1)	450 μm	233 μm	230 μm	135 μm
Width	47 μm	51 μm	28 μm	32 μm
Thickness	2.1 μm	1.5 μm	7.4 μm	5.2 μm
k_c	0.2 N/m	0.6 N/m	39 N/m	75 N/m
ω_0	14 kHz	36 kHz	189 kHz	373 kHz
Full length (L_2)	475 μm	262 μm	248 μm	142 μm

Four different rectangular cantilevers made of monocrystalline silicon²³ were examined. The data of the cantilevers are given in Table I. Length L_1 , width, thickness, spring constant, and resonance frequency were measured or calculated by the manufacturer. L_1 is the length from the mount to the sensor tip. As can be seen from the optical micrographs (Fig. 4), the full length L_2 of the cantilevers is slightly larger. Cantilevers 1 and 2 are relatively soft and thin compared to cantilevers 3 and 4. In all cantilevers the (110) direction is parallel to the length axis. The Young's modulus E of silicon in this direction is 1.69×10^{11} N/m² (Ref. 24) and the mass density ρ is 2330 kg/m³.

In a first experiment, the amplitude of the vibration modes was measured along the cantilever and compared with the theoretical values given by Eq. (8). In Figs. 5(a)–5(c) the squares and the solid line show the vibration amplitude measured with the interferometer for cantilever 2. The dashed

line represents the calculated amplitude. $L = 260 \mu\text{m}$ was assumed. In every graph, the amplitude was fitted using only one point on the graph. The clamped end of the cantilever is at $x = 0$. The mode $n = 1$ was not measured because its frequency is smaller than 100 kHz and hence below the cutoff frequency of the interferometer. A very good agreement between theory and experiment can be observed. Near the free cantilever end, the signal-to-noise ratio of the measured signal decreased because the laser spot was refracted by the sensor tip or by the edges of the cantilever.

From our measurements it becomes clear that the vibration spectrum of a cantilever cannot be measured without scanning the detection spot along the cantilever. Otherwise one might miss a mode because it accidentally might have a node at the spot position. The only position on the cantilever where all modes have a maximum of their vibration amplitude is the free end.

The exural vibration spectra of the four cantilevers are shown in Figs. 6(a)–6(d). The amplitude was measured in the maximum nearest to the free end. The excitation frequency was changed stepwise manually, and afterwards the spot position was readjusted slightly to find the maximum of the vibration amplitude. The modes with frequencies below 100 kHz could not be measured as mentioned above. For all cantilevers the spacing of the modes increases with increasing frequency and with increasing cantilever stiffness in accordance with theory. In Table II the experimental exural resonance frequencies f_{exp} are compared to the calculated f_n . The corresponding wavelength λ_n of the modes is also given,

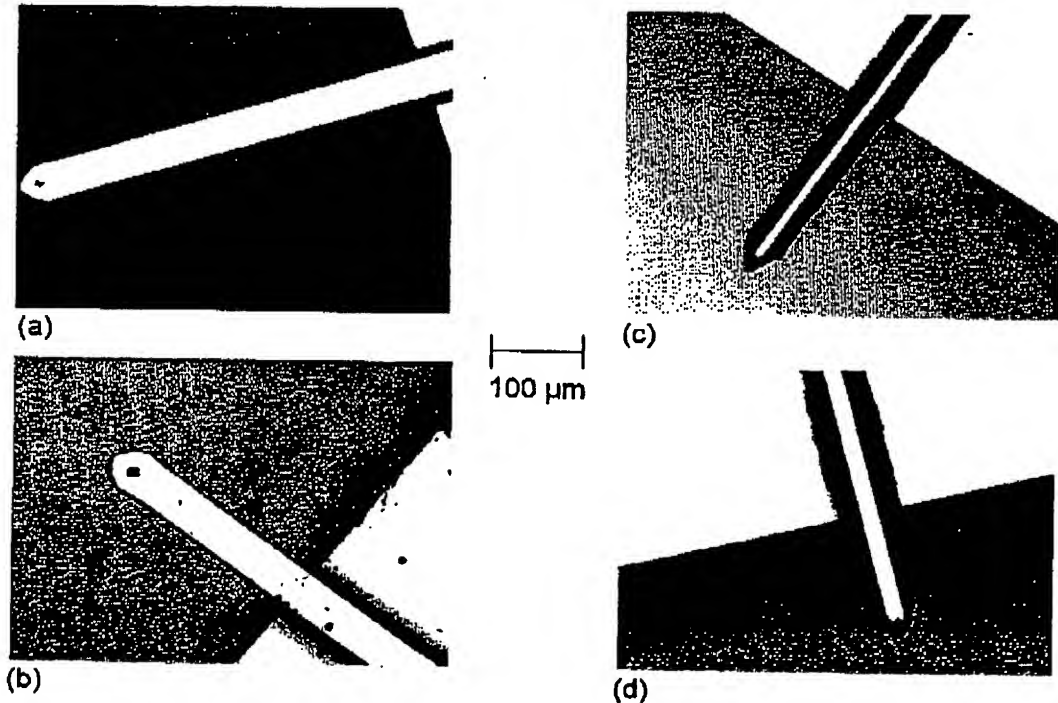


FIG. 4. Optical micrographs showing (a) cantilever 1, (b) cantilever 2, (c) cantilever 3, and (d) cantilever 4.

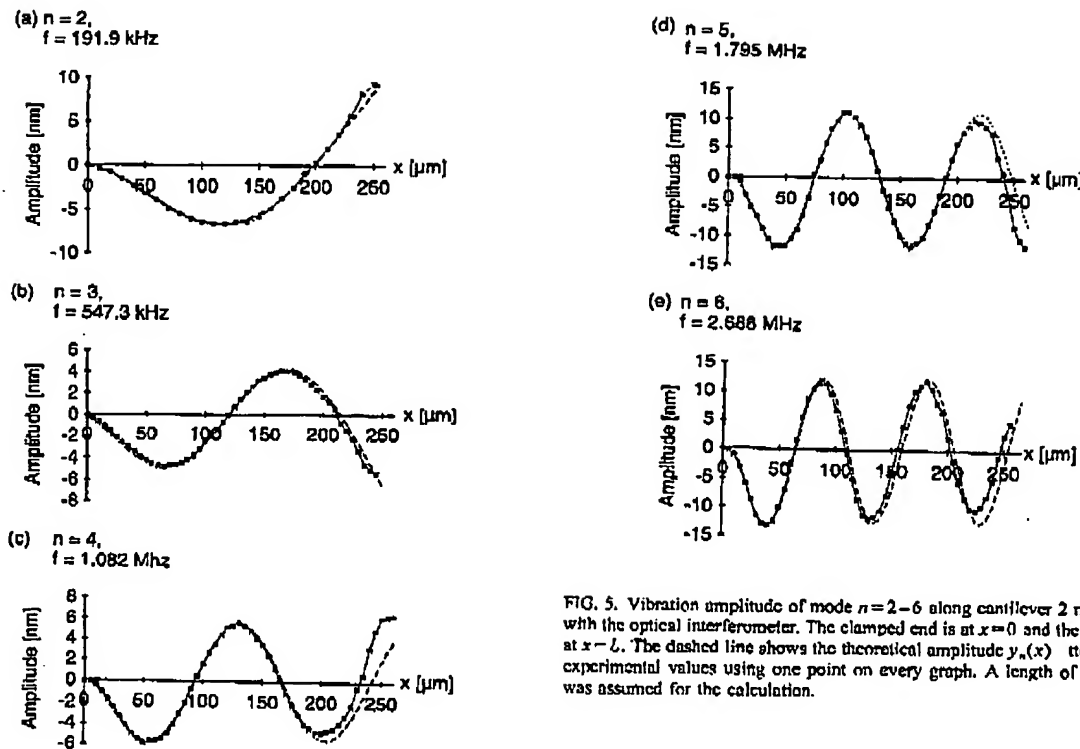


FIG. 5. Vibration amplitude of mode $n = 2-6$ along cantilever 2 measured with the optical interferometer. The clamped end is at $x = 0$ and the free end at $x = L$. The dashed line shows the theoretical amplitude $y_n(x)$ fitted to the experimental values using one point on every graph. A length of 260 μm was assumed for the calculation.

For all exural modes $f_{\text{exp}}/(k_n L)^2$ should give the constant value $1/c_c^2$ according to Eqs. (6) and (7).

Figure 7 shows the difference of $f_{\text{exp}}/(k_n L)^2$ from the average value in % for the four cantilevers. For cantilever 1 $f_{\text{exp}}/(k_n L)^2$ is almost perfectly a constant; only mode $n = 12$ obviously does not fit into the exural vibration spectrum. The vibrational spectrum of cantilever 2 also shows a good agreement between experiment and theory. The mode $n = 8$ could not be excited experimentally. The two stiff cantilevers 3 and 4, however, show an appreciable deviation from theory.

The mass of the sensor tip was not considered in the calculations. The sensor tip is a small cone of 15 μm height and 35° opening angle. Its mass m_{tip} is approximately 8×10^{-13} kg. This means that for all cantilevers the effective mass $m^* \approx m/4$ is more than one order of magnitude larger than m_{tip} .

Since in the elementary theory of exural vibration rotation and shear deformation of the cross sections are not taken into account, the phase velocity increases in nicely with increasing mode number. A theoretical description taking both effects into account leads to a phase velocity converging towards a value between the Rayleigh wave velocity and the bulk shear wave velocity.²⁵ However, as long as the cantilever thickness divided by the mode wavelength $b/\lambda < 0.1$, the elementary theory is in good agreement with the exact theory.²⁵ From Tables I and II one can see that this holds for all cantilever modes, even for the stiff cantilevers. The systematic deviation of the resonance frequencies of the stiff cantilevers is due to the cantilever shape. At the free end, no

uniform cross section is realized as assumed. Also, the cantilevers are not really clamped at $x = 0$ but continued as a sort of stripe waveguide on top of the chip which changes the boundary condition.

From the width of the resonance peaks Δf , the quality factor $Q = f_{\text{exp}}/\Delta f$ was calculated for all resonances and is shown in Fig. 8. For the cantilevers 1–3 Q has a maximum between 1 and 2 MHz. The damping of free AFM cantilevers is mainly caused by sound radiation and friction with air. In vacuum, the Q values of the AFM cantilevers are orders of magnitude higher than in air.⁸

As already discussed earlier, torsional vibrations must also be taken into account when analyzing AFM cantilever vibrations. If the cantilevers are slightly asymmetric, coupling between torsional and exural vibrations becomes possible. Mode coupling between a exural and a torsional mode probably happened when we tried to excite mode $n = 8$ of cantilever 2. When the excitation frequency was tuned to 5.05 MHz, the cantilever started to vibrate at the two neighboring frequencies of 2.35 and 2.7 MHz, whose sum is 5.06 MHz, instead of vibrating at its resonance around 5 MHz. The peak at 2.7 MHz can be assigned to the exural mode $n = 6$ which coupled to a torsional mode of 2.36 MHz resonance frequency. Also, the vibrational mode with the twelfth frequency which does not fit into the spectrum of cantilever 1 is probably a torsional mode. Since the torsional modes are equidistant in frequency while the spacing of the exural modes increases, the probability increases to excite a torsional mode at higher frequencies.

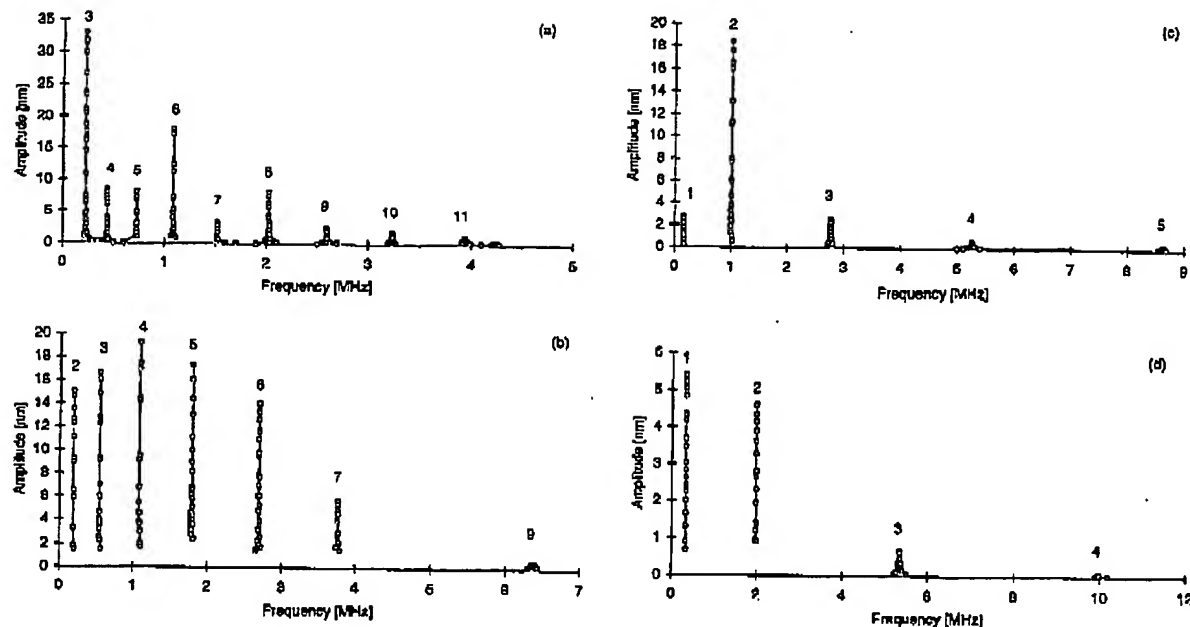


FIG. 6. Frequency spectra of (a) cantilever 1, (b) cantilever 2, (c) cantilever 3, and (d) cantilever 4 measured experimentally with the optical interferometer. The mode numbers n are indicated above the resonance peaks. Most of the resonance peaks appear as vertical lines because their line width is not resolved in the frequency scale used to display all measured resonances.

The comparison between experiment and theory for the fcc cantilever has shown that the exural vibration theory is sufficient to describe AFM cantilever vibrations in the frequency range we discussed here. Nevertheless, the geometry of the cantilevers plays an important role, and for the stiffer cantilevers a better agreement with experiment can probably only be achieved by calculating the modes numerically. In the special case regarded here, the mass of the tip could be neglected because it is very small compared to the cantilever mass. The first four to ten modes could be excited with high amplitude, with Q factors ranging from 90 to 905. This means that the higher modes are well suited for sensing purposes. Using the higher modes with many nodes, special care

has to be taken in order to choose the position along the cantilever on which the vibration amplitude is measured.

III. AFM CANTILEVER WITH ITS SENSOR TIP CONTACTING A SAMPLE SURFACE

A. Linear model for the cantilever vibrating with surface contact

When the cantilever is approached to a sample surface, in most cases the sensor tip senses first the long-range attractive tip-sample interaction forces such as Van der Waals forces. Using a soft cantilever, the tip jumps into contact with the sample surface into an equilibrium position, where the tip-sample interaction force is balanced by the cantilever

TABLE II. Experimentally determined eigenfrequencies f_{exp} of the four cantilevers used as compared to the frequencies f_n and wavelength's λ_n calculated from exural vibration theory.

n	$k_n L$	Cantilever 1			Cantilever 2			Cantilever 3			Cantilever 4		
		f_{exp} (MHz)	f_n (MHz)	λ_n (μm)									
1	1.875		0.013	1592		0.031	878	0.16305	0.157	831	0.33085	0.310	476
2	4.694		0.080	636	0.1919	0.195	351	1.0052	0.984	332	1.986	1.943	190
3	7.885	0.22385	0.226	379	0.547	0.550	209	2.762	2.775	198	5.337	5.482	113
4	10.996	0.4395	0.439	271	1.082	1.069	150	5.265	5.398	142	9.99	10.662	81
5	14.137	0.7279	0.726	211	1.795	1.767	116	8.64	8.922	110			
6	17.279	1.0869	1.084	173	2.6885	2.640	95						
7	20.420	1.518	1.514	146	3.76	3.686	81						
8	23.562	2.021	2.016	127		4.908	70						
9	26.704	2.593	2.590	112	6.39	6.305	62						
10	29.845	3.235	3.235	100									
11	32.987	3.94	3.952	90									
12	36.128	4.24	4.741	83									

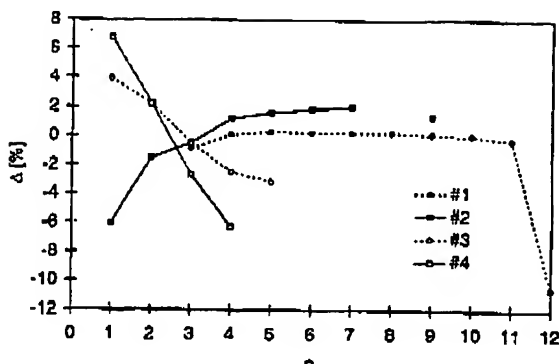


FIG. 7. Difference Δ in % of $f_{\text{exp}}/(k_c L)^2$ from its average value for the four cantilevers examined experimentally. For exural vibration modes $f_{\text{exp}}/(k_c L)^2$ should be a constant. This is the case for most of the resonance frequencies found for cantilevers 1 and 2 while the stiffer cantilevers 3 and 4 show a deviation from this behavior.

force. When an ultrasonic wave is coupled into the sample, such that the sample surface vibrates at ultrasonic frequencies, the sensor tip and the cantilever are also forced to vibrate around their equilibrium position. The tip-sample interaction forces are highly nonlinear. However, if only very small vibration amplitudes of the cantilever around its equilibrium position are excited, the tip-sample force can be expanded linearly, and it can be represented by a linear spring with spring constant k^* , where k^* is the negative derivative of the tip-sample force in the equilibrium position:²⁶

$$k^* = - \left. \frac{\partial F(\xi)}{\partial \xi} \right|_{\xi = \xi_e}. \quad (19)$$

Here ξ is the tip-sample distance, $F(\xi)$ is the tip-sample interaction force, and ξ_e is the equilibrium position.

The spring model is shown in Fig. 1(b). In the contact case, the forces exerted by the spring k^* are repulsive when the cantilever approaches the surface and attractive when it moves away from the surface. As can be seen in Fig. 1(b), it

is assumed that the AFM cantilever is positioned parallel to the sample surface, as a consequence the exural cantilever deflections are normal to the sample surface, i.e., in the ξ direction. Furthermore, it is assumed that the forces which act onto the sensor tip act as a point force on the free end of the cantilever. In the simple model used here, the cantilever is not deflected in its rest position. In the contact mode, the corresponding equilibrium position of the sensor tip can always be adjusted experimentally by moving the sample surface relative to the cantilever mount.

To analyze the behavior of this system, the resonance frequencies of a cantilever with one clamped end and the other end coupled to a spring must be calculated. The spring at the end changes the boundary conditions at $x=L$. Like the free end the spring-coupled end can transfer no moments. But a deflection y generates a force $-k^*y$ which has to be added to the shear force $EI \frac{\partial^3 y}{\partial x^3}$:

$$EI \frac{\partial^3 y}{\partial x^3} - k^*y = 0. \quad (20)$$

Therefore, the boundary conditions at $x=L$ are now

$$\frac{\partial^2 y}{\partial x^2} = 0, \quad \frac{\partial^3 y}{\partial x^3} = \frac{k^*}{EI} y = \frac{3k^*}{k_c L^3} y \quad \text{for } x=L. \quad (21)$$

The boundary conditions at $x=0$ are the same as in Eq. (4). Instead of using Eq. (2) it is more convenient for the calculation to express the general solution for the local amplitude (omitting the time dependence) in the following way:

$$y(x) = A(\cos kx + \cosh kx) + B(\sin kx - \sinh kx) \\ + C(\sin kx + \sinh kx) + D(\sin kx - \cosh kx). \quad (22)$$

The characteristic equation for this system is calculated in the same way as for the clamped-free cantilever by inserting the general solution and its derivatives into the boundary conditions and solving for the constants A , B , C , and D in the general solution. After some straightforward calculation one obtains

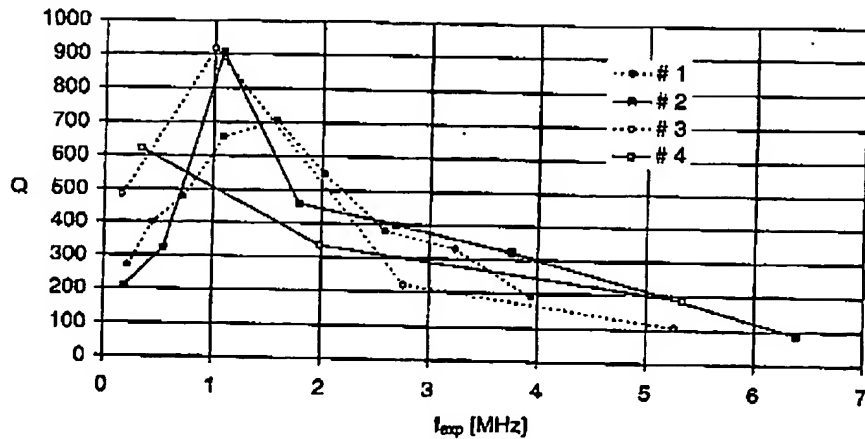


FIG. 8. Quality factor Q of the resonances shown in Figs. 6(a)–6(d). Q was calculated from the center frequency of the resonance divided by the width of the resonance.

TABLE III. Boundary conditions at $x=L$ and characteristic equations for the three different cases shown in Figs. 1(a)–1(c).

	Boundary conditions at $x=L$	Characteristic equation
(a) Free end (in nitely soft spring, $k^*=0$)	$\frac{\partial^2 y}{\partial x^2}=0$ $\frac{\partial^3 y}{\partial x^3}=0$	$\cos k_n L \cosh k_n L + 1 = 0$
(b) Spring- coupled end (contact mode, repulsive tip- sample forces)	$\frac{\partial^2 y}{\partial x^2} \approx 0$ $\frac{\partial^3 y}{\partial x^3} = \frac{k^*}{EI} y = \frac{3k^*}{k_c L} y$	$\sinh k_n L \cos k_n L - \sin k_n L \cosh k_n L$ $= \frac{(k_n L)^3 k_c}{3k^*} (1 + \cos k_n L \cosh k_n L)$
(c) Pinned end (in nitely stiff spring, $k^*=\infty$)	$y=0$ $\frac{\partial^2 y}{\partial x^2}=0$	$\sinh k_n L \cos k_n L - \sin k_n L \cosh k_n L = 0$

$$\sinh k_n L \cos k_n L - \sin k_n L \cosh k_n L \\ = \frac{(k_n L)^3 k_c}{3k^*} (1 + \cos k_n L \cosh k_n L). \quad (23)$$

Equation (23) reduces to Eq. (5) if $k^*=0$, i.e., if the spring is in nitely soft. In the other extreme case, when $k^*=\infty$ one obtains a cantilever pinned at one end [Fig. 1(c)].¹⁸ The boundary conditions at $x=L$ and the characteristic equation for the clamped-pinned cantilever are listed in Table III. The solutions of Eq. (23) were found numerically using *Mathematica*.²⁷ Some examples are listed in Table IV. In Fig. 9 the first three resonance frequencies f_n of a spring-coupled cantilever are shown as a function of k^*/k_c . f_n was normalized to the first resonance frequency of the clamped-free cantilever. The resonance frequency of every mode of the clamped-spring-coupled cantilever is between the resonance frequency of the clamped-free cantilever mode and the resonance frequency of the clamped-pinned cantilever mode. The open circles in Fig. 9 show the resonance frequency f_{n*} of the spring-coupled system normalized to the free resonance frequency f_0 as it is calculated from the point-mass model.²⁶

$$\frac{f_{n*}}{f_0} = \frac{\sqrt{\frac{k_c + k^*}{m^*}}}{\sqrt{\frac{k_c}{m^*}}} = \sqrt{\frac{k_c + k^*}{k_c}}. \quad (24)$$

If the tip-sample contact is softer than the cantilever spring constant, $k^* < k_c$, there is a good agreement between the point-mass model and the elastic beam model. However, if $k^* > k_c$, k_c becomes negligible compared to k^* in the point-mass model. This means that the system now behaves like a point mass m^* attached to a spring k^* and $f_{n*} \approx \sqrt{k^*/m^*}$. The elastic beam, however, can vibrate even if both ends are fixed. Therefore the point-mass model fails if $k^* > k_c$. The local vibration amplitudes of modes 1, 2, and 3 can be seen in Fig. 10. They were obtained using Eq. (8) and the $k_n L$ calculated from Eq. (23). For very soft springs the local vibration amplitudes are maximal at the end of the cantilever and increase compared to the clamped-free case. When the spring becomes stiffer, the slopes at the end of the cantilever go through zero and change their sign. If k^* increases further, the maximum of the vibration amplitudes is no longer at the end of the cantilever and the vibration amplitudes at the end decrease until they become zero in the clamped-pinned case. Note that the k^* which causes zero slope at the end increases with increasing mode number, i.e.,

TABLE IV. Solutions $k_n L$ of Eq. (23) obtained with *Mathematica* for different values of k^*/k_c . No solutions are given in cases where the difference between the clamped-free solution and the clamped spring-coupled solution is less than 0.001.

n	Free end ($k^*=0$)	$k^*/k_c=0.1$	$k^*/k_c=1$	$k^*/k_c=10$	$k^*/k_c=100$	$k^*/k_c=1000$	Pinned end ($k^*=\infty$)
1	1.8751	1.91891	2.2135	3.16765	3.82981	3.91704	3.9266
2	4.69409	4.69699	4.7234	5.00112	6.40415	7.00766	7.06358
3	7.85476	7.85538	7.86097	7.91896	8.58742	10.012	10.2102
4	10.9955	10.9958	10.9978	11.0185	11.2559	12.851	13.3518
5	14.1372	14.1373	14.1382	14.1479	14.2523	15.4765	16.4934
6	17.2788		17.2793	17.2846	17.3396	18.0795	19.635
7	20.4205			20.4239	20.4567	20.8774	22.7765
8	23.5619				23.5853	23.839	25.9181

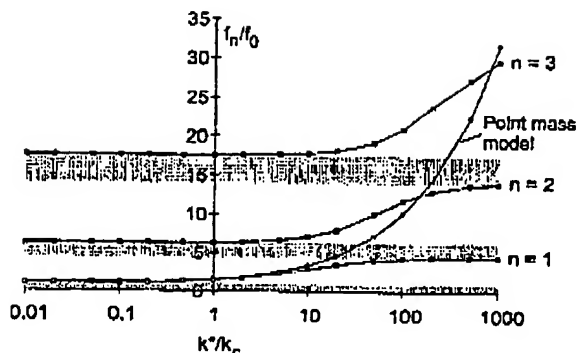


FIG. 9. Resonance frequencies f_n of the clamped spring-coupled system (black squares) normalized to the 1st resonance frequency of the clamped-free cantilever f_0 . As shown here for the 1st three modes, the resonance frequency of the n th mode of the clamped spring-coupled cantilever lies between the frequency of the n th clamped-free mode and the n th clamped-pinned mode. When k^*/k_c is increased from 0 to ∞ the resonance frequency of every mode shifts from the free case to the clamped case. The gray areas indicate frequency gaps. A comparison with the point-mass model for the cantilever (open circles) shows that this model predicts too large frequency shifts for $k^*/k_c > 1$.

a very soft spring has little influence on the higher modes, while a very stiff spring causes the lower modes to behave almost like in the pinned case.

Additionally to a frequency shift of the resonances one observes an increase in the damping when the sensor tip comes close to the sample surface. There also might be a

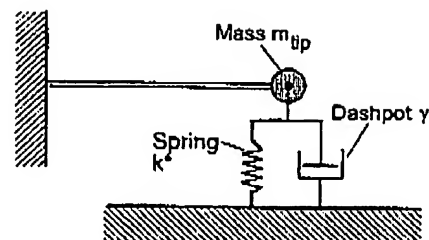


FIG. 11. Additionally to the forces between the sample surface and the sensor tip—represented by the spring, damping—represented by the dashpot—has to be considered. Also there might be a mass m_{tip} fixed to the end of the cantilever.

mass m_{tip} attached to the end of the cantilever. Both effects result in a modification of the forces at $x=L$ (Fig. 11) and therefore change the fourth boundary condition:

$$\frac{\partial^2 y}{\partial x^2} = 0, \quad \frac{\partial^3 y}{\partial x^3} = \frac{1}{EI} \left(k^* y + \gamma \frac{\partial y}{\partial t} + m_{tip} \frac{\partial^2 y}{\partial t^2} \right), \quad x=L. \quad (25)$$

γ is the damping constant, and a damping force proportional to the relative tip-sample velocity was assumed. The time derivatives in Eq. (25) can be calculated easily, and therefore the last boundary condition can be expressed as

$$\frac{\partial^3 y}{\partial x^3} = \frac{1}{EI} y(k^* + i\gamma\omega - m_{tip}\omega^2) \quad (26)$$

or, using Eq. (3),

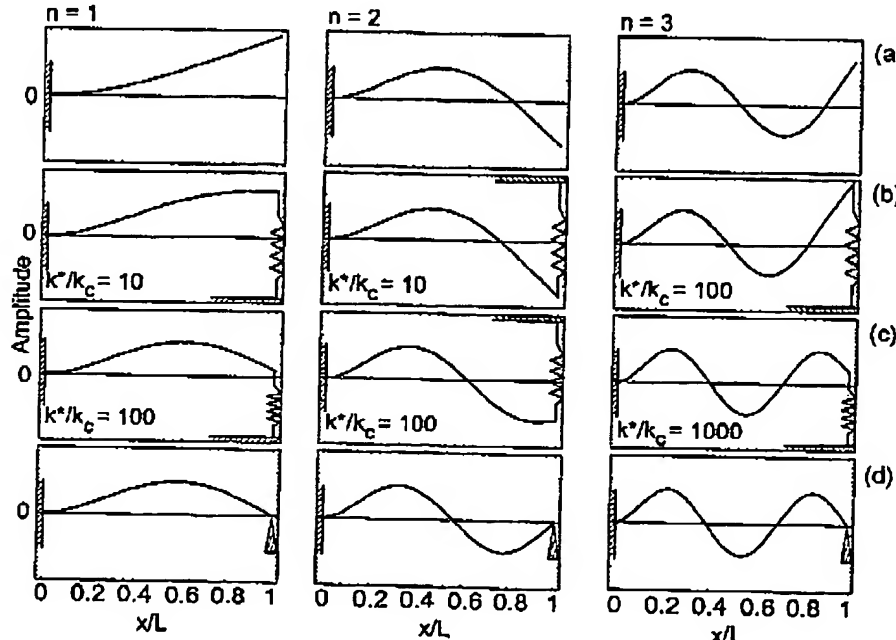


FIG. 10. Calculated local vibration amplitudes along a cantilever with rectangular cross section for mode $n=1, 2$, and 3 (from left to right) for different values of k^*/k_c (from top to bottom). Because of space, in the second column ($n=2$) the spring was drawn with its fixed end on top. The springs are always in their undeformed rest positions when the end of the cantilever is at zero. (a) In the clamped-free case the maximum of the vibration amplitudes is at the free end. (b) and (c) show the effect of a spring with increasing stiffness. (d) At the pinned end, the vibration amplitude of the cantilever becomes zero.

$$\frac{d^3y}{dx^3} = \varphi(k) \cdot y$$

with

$$\varphi(k) = \left(\frac{k^*}{EI} + i\gamma k^2 \sqrt{\frac{1}{EI\rho A}} - k^4 \frac{m_{tip}}{\rho A} \right). \quad (27)$$

The characteristic equation is then similar to Eq. (23):

$$\begin{aligned} \sinh k_n L \cos k_n L - \sin k_n L \cosh k_n L \\ = \frac{k_n^3}{\varphi(k)} (1 + \cos k_n L \cosh k_n L). \end{aligned} \quad (28)$$

This equation also gives the exact solutions for the free vibration frequencies ($k^* = 0, \gamma = 0$) of a cantilever with a mass at its end. In this case $\varphi(k)$ reduces to $\varphi(k) = -k^4 m_{tip}/\rho A = -k^4 L m_{tip}/m$ and the characteristic equation is

$$\begin{aligned} 1 + \cos k_n L \cosh k_n L = - \frac{m_{tip}}{m} \cdot k_n L (\sinh k_n L \cos k_n L \\ - \sin k_n L \cosh k_n L). \end{aligned} \quad (29)$$

To solve Eq. (29) only for the lowest wave number of the system, i.e., for small k , the trigonometric functions can be expanded in polynomial series:

$$\begin{aligned} 1 + \left(1 - \frac{(k_1 L)^2}{2!} + \frac{(k_1 L)^4}{4!} \right) \left(1 + \frac{(k_1 L)^2}{2!} + \frac{(k_1 L)^4}{4!} \right) \\ \approx - \frac{m_{tip}}{m} \cdot k_1 L \left[\left(k_1 L + \frac{(k_1 L)^3}{3!} \right) \left(1 - \frac{(k_1 L)^2}{2!} \right) \right. \\ \left. - \left(k_1 L - \frac{(k_1 L)^3}{3!} \right) \left(1 + \frac{(k_1 L)^2}{2!} \right) \right]. \end{aligned} \quad (30)$$

When all factors containing $k_1 L$ higher than the fourth power are neglected, the approximation for the lowest resonance frequency reduces to

$$k_1 L \approx \sqrt[4]{\frac{12}{1 + 4 \frac{m_{tip}}{m}}}. \quad (31)$$

This approximation is equivalent to Eq. (13) as can be seen when $(1.875)^4 \approx 12$ is inserted and $k_1 L$ is calculated from m_{tip} .

B. Cantilever vibrating in contact with a sample surface experiment

When the sensor tip contacts the sample surface, forced vibrations can be excited by sample surface vibrations. To examine the spectra of surface-coupled cantilevers experimentally, we used our atomic force acoustic microscope setup.^{5,16,28} A piezoelectric transducer was bonded to the sample with a coupling gel. We excited the transducer with an electrical spike, so that the sample surface movement was a short pulse containing a broad band of frequencies. The resulting cantilever vibration was measured with a knife-edge detector²⁹ and Fourier transformed. The sample was a thin glass plate partially covered with chromium. At high

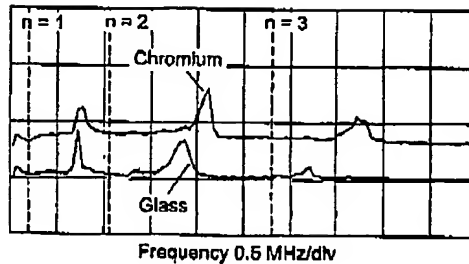


FIG. 12. Frequency spectra of cantilever 3 measured on top of a glass sample partially covered with chromium. The dashed lines show the resonance frequencies when the cantilever is free.

excitation voltages the cantilever vibration spectra contained many signals, but at very low exciting voltage most of the peaks disappeared and the remaining resonances could be assigned to the theoretical modes.

Figure 12 shows the spectra which were obtained with cantilever 3. The dashed lines are the free resonance frequencies which were measured in the experiment described in the previous section. In accordance with theory, the frequencies of all modes are higher in the contact case. In Table V(a) the resonance frequencies are listed. The frequency shift is larger on the chromium-covered parts of the sample than on the glass surface. Using Eqs. (6), (7), and (23), in principle k^* can now be calculated from the shifted resonance frequencies in the spectra:

TABLE V. Resonance frequencies of the spectra shown in Fig. 12 and corresponding k^* .

(a) Experimental resonance frequency of cantilever 3 on top of the glass sample partially covered with chromium. An accuracy of ± 5 kHz is assumed

Mode n	1	2	3
Frequency glass	675 kHz	1.825 MHz	3.175 MHz
Frequency chromium	725 kHz	2.075 MHz	3.675 MHz

(b) k^* calculated with the data given by the manufacturer: $c_e = 4.274 \times 10^{-3} \sqrt{s}$, modeled with spring at the end. The errors were calculated by varying the resonance frequencies by ± 5 kHz.

Mode n	1	2	3
k^* (N/m) glass	863 \pm 30	1617 \pm 17	-1850 \pm 60
k^* (N/m) chromium	1293 \pm 60	2703 \pm 28	1863 \pm 29

(c) k^* calculated with the data derived from the free vibration frequencies. Mode $n=1$: $c_e = (4.6437 \pm 0.001) \times 10^{-3} \sqrt{s}$; $n=2$: $c_e = (4.682 \pm 0.001) \times 10^{-3} \sqrt{s}$; $n=3$: $c_e = (4.7263 \pm 0.0005) \times 10^{-3} \sqrt{s}$

Mode n	1	2	3
k^* (N/m) glass	2644 \pm 350	2621 \pm 39	2234 \pm 28
k^* (N/m) chromium	-10527 \pm 8000	6046 \pm 165	5175 \pm 41

(d) k^* calculated with $L_1 = (230 \pm 5) \mu\text{m}$ ($c_e = (4.274 \pm 0.1) \times 10^{-3} \sqrt{s}$), and L_2 derived from the free resonance frequencies as in (c)

Mode n	1	2	3
k^* (N/m) glass	1005 \pm 130	3345 \pm 410	9198 \pm 3870
k^* (N/m) chromium	1428 \pm 170	4713 \pm 440	13901 \pm 5040

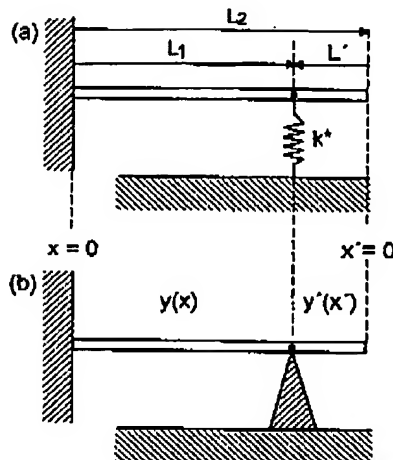


FIG. 13. Model for cantilevers with a sensor tip fixed at any length element of the beam. The cantilever can be divided into two parts with length L_1 and L' and individual solutions $y(x)$ and $y'(x')$, respectively. As in the simpler case with the spring at the end as shown in Figs. 1(a)–1(c), the spring-coupled boundary condition converges to the pinned boundary condition when $k^* \rightarrow \infty$.

$$k^* = k_c \cdot \frac{1 + \cos(c_c \sqrt{f_n}) \cosh(c_c \sqrt{f_n})}{\sinh(c_c \sqrt{f_n}) \cos(c_c \sqrt{f_n}) - \sin(c_c \sqrt{f_n}) \cosh(c_c \sqrt{f_n})} \cdot \frac{(c_c \sqrt{f_n})^3}{3} \quad (32)$$

Table V(b) shows the results which were obtained for k^* using the cantilever dimensions and k_c given by the manufacturer and in Table V(c) k^* was calculated using the free resonance frequencies measured experimentally to determine c_c . This comparison shows that the values obtained for k^* depend very sensitively on the geometrical dimensions of the cantilever inserted into Eqs. (7) and (23). As can be seen in Fig. 9, there are gaps in the frequency spectrum of an individual cantilever, i.e., frequencies which cannot be resonance frequencies of the clamped/spring-coupled system. Negative values for k^* are obtained when the experimental resonance frequency is in such a gap. The large errors in Table V(c) for mode $n=1$ on chromium are obtained because the tip-sample contact stiffness is much higher than the spring constant of the cantilever. Therefore, the frequencies of the lowest flexural vibration mode already converge towards the frequency of the clamped-pinned case, which means that small changes in resonance frequency correspond to very large changes in k^* . As pointed out above, a disagreement between the flexural wave theory and the experiment could be observed originating from the inhomogeneous cross section of the cantilever and from the boundary conditions at the clamped end. The fact that the sensor tip is not exactly at the end of the beam (see Fig. 4) can also cause frequency shifts which do not agree with the simple theory and a situation arises as shown in Fig. 13(a). Now the cantilever can be divided into two parts, the 1st part with length L_1 extending from the clamped end to the spring and the second part with

length L' extending from the spring to the free end. The full length of the cantilever is $L_2 = L_1 + L'$. The characteristic equation of this system is

$$\begin{aligned} & -(\cosh k_n L_1 \sin k_n L_1 - \sinh k_n L_1 \cos k_n L_1) \\ & \times (1 + \cos k_n L' \cosh k_n L') + (\cosh k_n L' \sin k_n L' \\ & - \sinh k_n L' \cos k_n L')(1 - \cos k_n L_1 \cosh k_n L_1) \\ & = 2 \cdot k_n^3 \frac{EI}{k^*} [1 + \cos k_n (L_1 + L') \cosh k_n (L_1 + L')]. \quad (33) \end{aligned}$$

A derivation of this equation is given in the Appendix. The results for k^* obtained with this equation using $L_1 = 230 \pm 5 \mu\text{m}$ and the free resonance frequencies to determine L_2 are shown in Table V(c). Now, no resonance frequency is in a gap, however, k^* increases with frequency for both, glass and chromium.

C. Calculation of K^* from Hertzian contact theory

To compare theory and experiment also for surface-coupled vibrations, the tip-sample interaction force must be known in order to calculate k^* . Especially when working in air, these forces are very complex and cannot be described in a simple way. A rough estimation of the order of magnitude for k^* can be obtained by using the formula for the Hertzian contact theory³⁰ when the tip penetrates into the sample surface. In the experiment, the force applied by the cantilever was adjusted to be negligible compared to the adhesion force. All attractive adhesion forces are summed in a force F_0 which is treated like an external force applied onto the tip. F_0 can be estimated from the so-called force calibration curves, where the tip is lowered until it is attracted by the sample surface and afterwards withdrawn until it detaches. The Hertzian contact force is

$$F_H = \frac{4E^*}{3} \sqrt{(-\xi)^3 R} \quad (34)$$

with

$$\frac{1}{E^*} = \frac{1 - \nu_t^2}{E_t} + \frac{1 - \nu_s^2}{E_s}, \quad (35)$$

where R is the radius of the sensor tip and E^* is the effective Young's modulus of the tip-sample contact. E_t , ν_t , E_s , and ν_s are the Young's moduli and the Poisson ratio of the tip and the surface, respectively. The equilibrium position ξ_e is calculated from

$$\frac{4E^*}{3} \sqrt{(-\xi_e)^3 R} - F_0 = 0 \Rightarrow -\xi_e = \left(\frac{3F_0}{4E^*} \right)^{2/3} R^{-1/3}. \quad (36)$$

Calculating the derivative of Eq. (34) and inserting Eq. (36) yields

$$\left. \frac{\partial F_H}{\partial \xi} \right|_{\xi=\xi_e} = -3\sqrt{6 \cdot E^{*2} \cdot R \cdot F_0} \quad (37)$$

and this means that

$$k^* = 3\sqrt{6 \cdot E^{*2} \cdot R \cdot F_0}. \quad (38)$$

The sensor tip is oriented in the $\langle 100 \rangle$ direction. The Young's modulus and Poisson ratio of silicon in this direction are 1.3098×10^{11} N/m² and 0.181, respectively.³¹ The Young's modulus of glass ranges from $(0.4-0.9) \times 10^{11}$ N/m² and the Poisson ratio is 0.2.³² For the Young's modulus of chromium such different values as 1.32 and 2.53×10^{11} N/m² can be found in the literature.^{32,33} The Poisson ratio is 0.3. The effective elasticity E^* for the sensor tip on the glass surface is therefore $E^* = (3.2-5.5) \times 10^{10}$ N/m² and the effective elasticity for the sensor tip on chromium is $(7.0-9.1) \times 10^{10}$ N/m². To calculate k^* the sensor tip radius R and the adhesion force F_0 are needed. The radius of curvature of fresh sensor tips used in our experiments is 10 nm. However, the radius probably became larger when the tips were used for some time, especially when they were vibrating on a stiff sample surface. From the smallest features which can be imaged with our tips, however, it can be concluded that R cannot be larger than 100 nm. F_0 varies in our experiments in air typically from 5×10^{-8} to 5×10^{-7} N. When all the uncertainties are considered, k^* can range from 145 to 973 N/m on glass and from 245 to 1355 N/m on chromium according to Hertzian contact theory.

Comparing these results from Hertzian contact theory to the experimental stiffness in Tables V(b)-V(d), it can be seen that the result for mode $n=1$ in Table V(b) agrees roughly with the upper limit for k^* calculated from Hertzian theory. However, the other two modes yield different results, even one with a negative value. Using the constants derived from the free resonance frequencies, one obtains roughly the same k^* for all three modes, as shown in Table V(c). Only on chromium the resonance frequency of mode $n=1$ yields a negative value for k^* . For glass and chromium the experimental k^* in Table V(c) is more than two times higher than the upper limit from Hertzian theory. If one takes into account that the sensor tip is not at the end of the cantilever, k^* again becomes smaller and therefore closer to the theoretical values at $n=1$ [Table V(d)], but now k^* increases with mode number (or frequency).

IV. DISCUSSION

The comparison has shown that the frequency shift of the resonances caused by the tip-sample contact elasticity depends very much on the geometry of the cantilever. Because the geometry of the cantilever plays such an important role for the determination of elastic constants of a sample surface, cantilevers with a simpler and better defined geometry are needed. It is important that a stiff clamp is realized also for the stiffer cantilevers, that the beam cross section is uniform, and that the sensor tip is at the end of the cantilever. A numerical characterization would be too time consuming because of the limited life span of each cantilever.

On the other hand, it is very possible that the stiffness of the upper surface layer penetrated by the sensor tip is higher than the values calculated from the bulk elastic moduli of the materials. In further experiments and calculations, the influence of damping forces will be examined. More precise contact mechanical models considering adhesion forces have to be used. However, it is possible that macroscopic models which treat the sensor tip as an homogeneous elastic body

and which consider no plastic deformation and material transfer between tip and surface do not describe the contact of a sensor tip of a few nanometers of radius accurately. One main problem in atomic force microscopy is the unknown shape of the sensor tip. From changes in image contrast we conclude that sensor tips change their shape when they are used in the contact mode. Stiff materials such as silicon are more likely to break than to be plastically deformed. If, for example, the silicon sensor tip used in the ultrasonic contact mode was broken, the spherical shape of the sensor tip was lost and the high measured contact stiffness might have been caused by a larger contact area than the one which was calculated from the assumed spherical shape of the tip.

Furthermore it has to be kept in mind that knife-edge and beam-deection detectors measure the local deection and not the amplitude. A full characterization of the cantilever vibration in contact with a sample surface could only be obtained by scanning the cantilever with an interferometer similar to the experiments we performed with free cantilevers in order to measure the calibrated local vibration amplitude along the x axis. The accuracy in the measurement of the contact resonances can be improved by exciting narrow band signals at well defined frequencies instead of Fourier transforming only one pulse containing a broad band of frequencies.

ACKNOWLEDGMENTS

The authors thank S. Hirsekorn and G. A. D. Briggs for helpful discussions. This research was partially supported by a grant from the European Union within the Human Capital and Mobility program.

APPENDIX: CALCULATION OF THE CLAMPED/SPRING-COUPLED SYSTEM WITH THE SPRING FIXED AT A GIVEN LOCATION ALONG THE CANTILEVER

As shown in Figs. 13(a) and 13(b) the cantilever can be divided into two parts. The first part extends from the clamped end at $x=0$ to the spring at $x=L_1$; the second part extends from the free end at $x'=0$ to the spring at $x=L'$. The full length of the cantilever is $L_2=L_1+L'$. The origin of the x' axis is chosen to be at the free end to simplify the calculation. The vibration amplitude is labeled $y(x)$ for the first part and $y'(x')$ for the second part, respectively. The boundary conditions for $y(x)$ are $y(0)=0$ and $\partial y/\partial x(0)=0$ at the clamped end and the boundary conditions for $y'(x')$ are $\partial^2 y'/\partial x'^2(0)=0$ and $\partial^3 y'/\partial x'^3(0)=0$ at the free end. Solutions for the whole cantilever can be found from tying $y(x)$ and $y'(x')$ together at the length element $x=L_1$ and hence $x'=L'$, taking into account the boundary conditions. To calculate the characteristic equation in this way is straightforward but a tedious task and therefore omitted here. However, it is much simpler to calculate the characteristic equation for the situation shown in Fig. 13(b), where the spring is replaced by a pin, and where $y(L_1)=y'(L')=0$ at the pin. In this case,

$$y(x)=B(\cos kx - \cosh kx) + D(\sin kx - \sinh kx), \quad (A1)$$

$$y'(x') = A'(\cos kx' + \cosh kx') + C'(\sin kx' + \sinh kx') \quad (A2)$$

with

$$\frac{B}{D} = -\frac{\sin kL_1 - \sinh kL_1}{\cos kL_1 - \cosh kL_1}$$

and

$$\frac{A'}{C'} = -\frac{\sin kL' + \sinh kL'}{\cos kL' + \cosh kL'}$$

At the length element where $x=L_1$, and $x'=L'$ the following boundary conditions have to be fulfilled:

$$\frac{\partial y}{\partial x}(L_1) = -\frac{\partial y'}{\partial x'}(L'), \quad (A3)$$

$$\frac{\partial^2 y}{\partial x^2}(L_1) = \frac{\partial^2 y'}{\partial x'^2}(L'). \quad (A4)$$

The third derivatives need not be equal because the difference of the forces exerted by the two parts of the cantilever beam are carried by the pin. When the derivatives of Eqs. (A1) and (A2) are inserted into Eqs. (A3) and (A4), one obtains the characteristic equation of a cantilever pinned at any position along its length axis:

$$\begin{aligned} & (\cosh k_n L_1 \sin k_n L_1 - \sinh k_n L_1 \cos k_n L_1)(1 + \cos k_n L' \\ & \times \cosh k_n L') - (\cosh k_n L' \sin k_n L' \\ & - \sinh k_n L' \cos k_n L')(1 - \cos k_n L_1 \cosh k_n L_1) = 0. \end{aligned} \quad (A5)$$

In Eq. (23), the characteristic equation of the clamped-pinned case and the characteristic equation of the clamped-free case are coupled by the factor $E/k_n^3/k^* = (k_n L)^3 k_c/3k^*$. In the situation treated now when $k^* \rightarrow 0$, the cantilever vibrates like a clamped-free cantilever with length $L_2 = L_1 + L'$ and the wave numbers k_n of the cantilever are given by

$$1 + \cos k_n(L_1 + L') \cosh k_n(L_1 + L') = 0. \quad (A6)$$

The characteristic equation for the clamped-pinned case is given in Eq. (A5). This means that the characteristic equation for the clamped-spring-coupled case is analogous to Eq. (23):

$$\begin{aligned} & (\cosh k_n L_1 \sin k_n L_1 - \sinh k_n L_1 \cos k_n L_1) \\ & \times (1 + \cos k_n L' \cosh k_n L') \\ & - (\cosh k_n L' \sin k_n L' - \sinh k_n L' \cos k_n L') \\ & \times (1 - \cos k_n L_1 \cosh k_n L_1) \\ & = A \cdot k_n^3 \frac{EI}{k^*} [1 + \cos k_n(L_1 + L') \cosh k_n(L_1 + L')]. \end{aligned} \quad (A7)$$

The value of the factor A can be found by considering the case $L' \rightarrow 0$, i.e., if the spring is moved to the end of the cantilever. Only if $A = -2$, Eq. (A7) is equal to Eq. (23). When damping and the mass of the sensor tip are to be considered, k^*/EI can be replaced by $\varphi(k)$ as in Eqs. (27) and (28).

- ¹G. Binnig, C. F. Quate, and C. Gerber, Phys. Rev. Lett. 56, 930 (1986).
- ²P. Maivald, H. J. Butt, S. A. Gould, C. B. Prater, B. Drake, J. A. Gurley, V. B. Elings, and P. Hansma, Nanotechnology 2, 103 (1991).
- ³V. B. Elings and J. Gurley, U.S. Patent No. 5,266,801 (1993).
- ⁴K. Yamamoto, H. Ogiso, and O. Kulakov, Appl. Phys. Lett. 64, 178 (1994).
- ⁵U. Rabe and W. Arnold, Appl. Phys. Lett. 64, 1493 (1994).
- ⁶B. Cretin and F. Stihl, Appl. Phys. Lett. 62, 829 (1993).
- ⁷D. Sarid, *Scanning Force Microscopy* (Oxford University, Oxford, 1991).
- ⁸M. Nonnenmacher, Ph.D. thesis, Gesamthochschule Kassel, Fachbereich Physik, Kassel, Germany (1990).
- ⁹M. Dreiter, D. Anselmetti, T. Richmond, U. Dammer, and H.-J. Güntherodt, Appl. Phys. Lett. 76, 5095 (1995).
- ¹⁰S. C. Minne, S. R. Manalis, A. Atalar, and C. F. Quate, Appl. Phys. Lett. 68, 1427 (1996).
- ¹¹D. F. L. Jenkins, M. J. Cunningham, W. W. Clegg, and M. M. Bokush, Meas. Sci. Technol. 6, 160 (1995).
- ¹²J. E. Sader, I. Larson, P. Mulvaney, and L. R. White, Rev. Sci. Instrum. 66, 3789 (1995).
- ¹³M. Sasaki, K. Hane, S. Okuma, and Y. Beisho, Rev. Sci. Instrum. 65, 1930 (1994).
- ¹⁴J. M. Neumeister and W. A. Ducker, Rev. Sci. Instrum. 65, 2527 (1994).
- ¹⁵G. Y. Chen, R. J. Warmack, T. Thundat, D. P. Allison, and A. Huang, Rev. Sci. Instrum. 65, 2532 (1994).
- ¹⁶H.-J. Butt and M. Juschnik, Nanotechnology 6, 1 (1995).
- ¹⁷P. M. Morse and K. U. Ingard, *Theoretical Acoustics* (McGraw-Hill, New York, 1968).
- ¹⁸W. F. Stokey, in *Shock and Vibration Handbook*, edited by C. M. Harris and C. E. Crede (McGraw-Hill, New York, 1976), pp. 7-1ff.
- ¹⁹L. Cremer and M. Heckl, *Körperschall* (Springer, Berlin, 1967).
- ²⁰O. Marti and J. Colchero, in *Forces in Scanning Probe Methods*, edited by H.-J. Güntherodt, D. Anselmetti, and R. Meyer (Kluwer Academic, London, 1995), p. 151ff.
- ²¹B. Cretin and D. Hauden, in *Proceedings of the IEEE Ultrasonics Symposium*, edited by B. R. McAvoy (1984), p. 656.
- ²²H. Peukert, M. Paul, S. Fassbender, R. Herzler, and W. Arnold (unpublished).
- ²³NanoSensors, Dr. Olaf Wolter GmbH, Wacholderweg 8, D 71134 Aalen, Germany.
- ²⁴O. Ohlsson (private communication).
- ²⁵E. Skudrzyk, *Simple and Complex Vibratory Systems* (The Pennsylvania State University, University Park, 1968).
- ²⁶U. Rabe and W. Arnold, Ann. Phys. 3, 589 (1994).
- ²⁷S. Wolfram, *Mathematica, A System for Doing Mathematics by Computer*, Wolfram Research Inc., 100 Trade Center Drive, Champaign, Illinois, 61820-7237.
- ²⁸U. Rabe, K. Janser, and W. Arnold, in *Proceedings of the 22nd International Symposium on Acoustic Imaging, Florence*, edited by P. Tortoli (Plenum, New York, to be published).
- ²⁹R. L. Whitman and A. Korpel, Appl. Opt. 8, 1567 (1969).
- ³⁰J. L. Lubkin, in *Handbook of Engineering Mechanics*, edited by W. Flügge (McGraw-Hill, New York, 1962), p. 42ff.
- ³¹S. Hirschorn (private communication).
- ³²F. Kohlrausch, *Praktische Physik* (Teubner, Stuttgart, 1968), Vol. 3.
- ³³Landolt-Bornstein, *Zahlenwerte und Funktionen*, Vol. IV/2a: *Stoffwerte und Verhalten von Metallischen Werkstoffen*, edited by H. Borchers, H. Hausinger, K.-H. Hellwege, K. L. Schäfer, and E. Schmidt (Springer, Berlin, 1964).